Computational Insights into the Binding of Pimodivir to the Mutated PB2 Subunit of the Influenza A Virus

Muhammad Arba[1,*], *Aprilia Surya Ningsih*[1], *La Ode Santiaji Bande*[2], *Setyanto Tri Wahyudi*[3], Candice Bui-Linh[4], Chun Wu[4,5] *and Amir Karton*[6,*]

[1]*Department of Pharmaceutical Analysis and Medicinal Chemistry, Faculty of Pharmacy, Universitas Halu Oleo, Kendari 93232, Indonesia*; muh.arba@uho.ac.id
[2]*Faculty of Agriculture, Universitas Halu Oleo, Kendari 93232, Indonesia*
[3]*Department of Physics, IPB University, Bogor 16680, Indonesia*
[4]Department of Biological-Biomedical Sciences, [5]Department of Chemistry & Biochemistry, College of Science and Mathematics, Rowan University, Glassboro, New Jersey 08028, United States
[6]*School of Science and Technology, University of New England, Armidale NSW 2351, Australia; amir.karton@une.edu.au*
***** *Correspondence: muh.arba@uho.ac.id (MA), amir.karton@une.edu.au* (AK)

Abstract

Influenza A virus (IAV) is reported to develop Pimodivir resistance because of multiple mutations within the Polymerase basic 2 protein (PB2) of IAV. The lack of a high-resolution structure of these PB2 mutants complexed with Pimodivir hinders efforts to understand the drug resistance. Here we decipher the binding differences of Pimodivir in the wild-type and mutant systems Q306H, S324I, S324N, S324R, F404Y, and N510T of IVA PB2 using homology modeling, molecular dynamics, molecular docking, and density functional theory simulations. The key residues responsible for Pimodivir binding were identified as Glu361, Arg355, Arg332, His357, and Phe323. Those mutations, mainly N510T, result in significant conformational changes of Pimodivir in the PB2 active site. As a result, the affinity of Pimodivir is significantly reduced in the N510T system. The mutation effects are less pronounced in the other mutant systems. Dynamic cross-correlation matrix (DCCM) analyses suggests that the single-point mutation N510T produces an allosteric effect on the ligand-binding domain, thus reducing ligand binding affinity. The present study reveals how a single-point mutation modulates the Pimodivir binding in IAV PB2, which provides important insights into designing new Pimodivir analogues with better binding affinities.

Keywords: Influenza virus A; Drug resistance; Polymerase basic 2 protein; Drug binding; Molecular dynamics simulations; Energy decomposition analysis; Molecular Docking simulations.

Introduction

Influenza, caused by influenza viruses, is an acute respiratory infection of a potentially deadly disease that infects around one billion people each year, with hundreds of thousands of deaths around the globe [1]. The burden of influenza exists in spite of available vaccines, and due to the current coronavirus-2019 pandemic, influenza severely complicates healthcare delivery. The influenza virus can be transmitted through the air via droplets that are expelled when an infected person talks, coughs or sneezes, as well as by touching a surface contaminated with the virus and then touching the mouth, nose, or eyes. Symptoms of influenza commonly include fever, cough, sore throat, runny or stuffy nose, body aches, headache and fatigue. In some cases, vomiting and diarrhea may also occur. Although influenza is a self-limited illness for most people, it can be serious or even deadly in certain populations such as young children, elderly individuals and individuals with underlying health conditions. Although vaccination has become the mainstay of efforts to prevent and minimize the impact of influenza, it is associated with variable influenza virus antigens [2]. Thus, effective antivirals targeting the virus could be a key to controlling the impact of influenza and reducing morbidity and mortality [2, 3].

Influenza virus is grouped into four types based on their core proteins, type A (influenza virus A; IAV), type B (influenza virus B; IBV), type C (influenza virus C; ICV), and type D (influenza virus D; IDV) [4, 5]. Among the four genera, IAV is the most pathogenic to people, and it can be transmitted between species [6].

The RNA-dependent RNA polymerase (RdRp) of IAV, which is highly conserved among influenza viruses, is one of the most attractive drug targets to treat IAV as it plays a crucial role in genom replication and transcription [7]. The RdRp consists of three protein subunits, i.e., polymerase acid protein (PA) with endonuclease activity, polymerase basic protein 1 (PB1) with polymerase activity, and polymerase basic protein 2 (PB2) containing five prime-cap binding sites (CBS) [5, 7, 8]. They are all closely related and responsible for replication and transcription of the viral RNA genome in the infected cell [9]. The polymerase synthesizes viral RNA through cap-snatching mechanism, which is not available in human cells. The viral RNA does not have a cap bound to it as IAV does not encode guanylyl transferase, and as a result, protein translation using host cell machinery does not occur. The virus, however, steals the host five-prime cap through cap-snatching mechanism in which the host primer cap binds to the PB2 cap-binding site, followed by cleavage of nucleotides from the host five-prime cap by PA, and concludes by RNA synthesis by PB1 [5, 10, 11].

The PB2 protein is considered a prime target for the development of new antiviral drugs because it has a crucial role in viral replication. Inhibition of PB2 function can effectively prevent the replication of the influenza virus, making it a promising target for antiviral drug development. The structure of PB2 consists of three domains: the N-terminal domain, the cap-binding domain, and the C-terminal domain. The N-terminal domain contains a flexible linker region that connects it to the cap-binding domain, while the C-terminal domain is involved in interaction with other components such as the polymerase acidic protein (PA) and the polymerase subunit basic protein 1 (PB1), forming a heterotrimeric complex. The cap-binding domain of PB2 is responsible for the recognition and binding of the 5' cap structure of host pre-mRNAs. This allows the influenza virus to hijack the host cell's machinery and use it for its replication. The ability of PB2 to recognize and cleave the host mRNA's 5' end is necessary for transcription of viral genes. Furthermore, targeting PB2 with antiviral drugs is believed to have broader-spectrum activity against various strains of influenza viruses rather than focusing on one particular strain. Recent studies have shown promising potential benefits of targeting PB2 for the development of broad-spectrum antiviral drugs that can tackle various strains of influenza viruses.

Polymerase basic protein 2 (PB2) is an essential protein for the influenza virus. It plays a crucial role in viral replication by binding to the host cell's mRNA cap structure, which is essential for the transcription of influenza virus RNA (Lemaire et al., 2017). This process is known as cap-snatching where PB2 cleaves the 5' end of host pre-mRNAs and uses them as primers to initiate the transcription of viral mRNA.

The R251K Substitution in Viral Protein PB2 Increases Viral Replication and Pathogenicity of Eurasian Avian-like H1N1 Swine Influenza Viruses

The R251K Substitution in Viral Protein PB2 Increases Viral Replication and Pathogenicity of Eurasian Avian-like H1N1 Swine Influenza Viruses

Kinase inhibitor roscovitine as a PB2 cap-binding inhibitor against influenza a virus replication

The most advanced drug targeting PB2, pimodivir, received its fast designation approval from the US Food and Drug Administration (FDA) in 2017 [12, 13, 14]. It blocks the cap-snatching activity of polymerase and inhibits the binding of host mRNA to PB2, thus preventing the early stage of viral transcription [2], and is particularly active against IAV [13].

Pimodivir extensively interact with the the cap-binding domain of PB2, which acts as a virulence determinant [2, 15, 16]. However, recent findings revealed that resistance against pimodivir emerged due to mutations on PB2. In vitro tests of pimodivir against IAV revealed the existence of mutations including Q306H, S324I, S324N, S324R, F404Y, and N510T, which resulted in decreased susceptibility of pimodivir [2, 12, 14, 17, 18, 19]. The present study aims to understand at the molecular level how the mutations affect pimodivir binding by employing molecular dynamics (MD) and density functional theory (DFT) simulations. Molecular dynamics simulation is a powerful to understand the details of protein-ligand interaction during a period of time, while the density functional theory offer more accuracy in describing protein-ligand in atomic details [20, 21]. These two complementary computational chemistry approaches provide valuable insights into the binding dynamics, structural, and energetic properties involved in protein-ligand interactions [20, 21, 22, 23, 24, 25, 26].

Computational Details

We applied virtual screening protocols comprising multiple filters with different scoring functions, including extra precision (XP) docking, molecular dynamics simulation, and MM-GBSA calculations to study pimodivir binding to WT and mutant proteins.

Protein structure preparation. The PDB structure of pimodivir in complex with PB2 was downloaded from the RCSB Protein Data Bank with PDB ID 5FMM, resolution 2.40 Å [27]. Water molecules and non-interacting ions were removed, and hydrogen atoms were added to the protein. The structure was then prepared using the Maestro's Protein Preparation Wizard,[28] via the addition of residue missing atoms, determination of the optimal protonation states for histidine residues, assignment of the correct potentially transposed heavy atoms in arginine, glutamine, and histidine side chains, optimization of the protein's hydrogen bond network, and a restrained minimization was carried out using the OPLS_2005 force field [29]. The prepared structure of PB2 was shown in Figure 1.

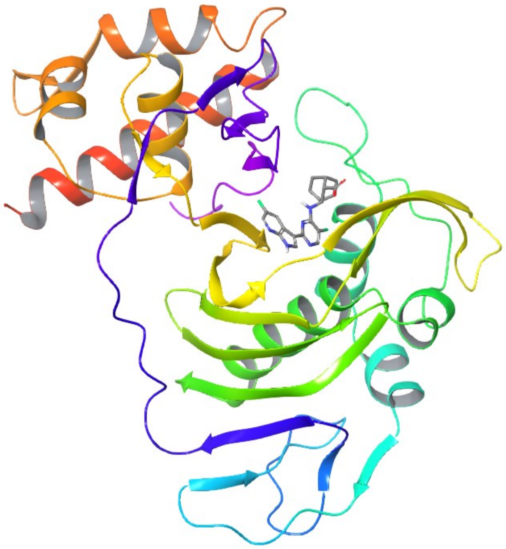

Figure 1. The prepared structure of PB2.

The mutant protein structures including Q306H, S324I, S324N, S324R, F404Y, and N510T were then each prepared by introducing the point mutation to the WT system using the protein preparation wizard [30] of Maestro 10.3 [31].

Pimodivir was prepared using Maestro including generating ionization states at pH = 7 by using Epik's pKa calculations[28]. The lowest tautomeric state of Pimodivir was selected and was then optimized to minimize the potential energy to relax any of the bad contacts using default parameters (Force field: OPLS3; Method: PRCG; Maximum iterations: 2500; Gradient convergence threshold: 0.5) [32]. The receptor grid file was built using the prepared merged protein-ligand complex, in which a van der Waals scaling factor of 1 and a partial charge cutoff of 0.25 were used. The binding site for Pimodivir was built based on the native ligand position. The optimal molecular structure of Pimodivir was then docked into the built grid of the protein receptor using OPLS3 force field with XP precision into the WT, Q306H, S324I, S324N, S324R, F404Y, and N510T receptor protein structures. The default parameters of the scoring function was used: ligand sampling was flexible, with sample nitrogen-inversions, same ring conformations, and bias sampling of torsions for amides which only penalized nonpolar conformations and added Epik state penalties to the docking score [33, 34, 35].

Molecular dynamics simulations. Due to reasons of computational cost, only residues 251 to 522 of the protein were considered in the MD simulations. Each protein-ligand pair was used to construct an MD simulation system. Na^+ ions were added to a concentration of 0.15 M NaCl to neutralize the systems. The OPLS_2005 force field, which was known for its accurancy for modeling protein-ligand complex was used to model the systems[36, 37]. All MD simulations were run using the Desmond simulation package[38]. The systems were relaxed using a relaxation protocol consisting of the following stages. (1) Brownian dynamics simulation under a constant number of atoms, volume, and temperature (NVT) ensemble at temperature 10 K for 100 ps. (2) Simulation under NVT ensemble at temperature 10 K with restraints on solute heavy atoms for 12 ps. (3) Simulation under NVT ensemble at temperature 10 K and restraints on solute heavy atoms for 12 ps. (4) Simulation under a constant number of atoms, pressure, and temperature (NPT) ensemble with temperature 10 K, pressure 1 bar, and restraints on solute heavy atoms for 12 ps. (5) Simulation under NPT with temperature 310 K, pressure 1 bar, and no restraints for 1.5 ns. A 100 ns production run was carried out under the NPT ensemble using the default protocol. The temperature was controlled using the Nosé-Hoover chain coupling scheme[39] with a coupling constant of 1.0 ps. The pressure was controlled using the Martyna-Tuckerman-Klein chain coupling scheme[39] with a coupling constant of 2.0 ps. M-SHAKE[40] was applied to constrain all bonds connecting hydrogen atoms, enabling a 2.0 fs time step in the simulations. The k-space Gaussian split Ewald method[41] was used to treat long-range electrostatic interactions under periodic boundary conditions (charge grid spacing of ~1.0 Å, and direct sum tolerance of 10^{-9}). The cutoff distance for short-range non-bonded interactions was set to 10 Å, and the long-range van der Waals interactions were based on a uniform density approximation. To reduce the computation, non-bonded forces were calculated using an r-RESPA integrator [42], where the short-range forces were updated every step, and the long-range forces were updated every three steps. Frames were saved at 50.0 ps intervals for analysis.

Simulation analysis. To check the convergence of the MD simulations, Cα protein and ligand RMSDs were computed over the whole trajectory. The plots depict structural variation over 100 ns, providing evidence that the convergence is reached. Using the Desmond trajectory clustering tool [43], clustering analysis was performed to obtain the most abundant structure of the complex. Backbone RMSD was used as the structural similarity, with the merging distance cutoff set at 2.5 Å. Hierarchical clustering with average linkage as the clustering method was employed. The structure with the greatest number of neighbors in the structural family, called the centroid structure, was used for representation.

MM-GBSA binding energy calculations. Molecular Mechanism-General Born Surface Area (MM-GBSA) binding energies were calculated for each protein-ligand system. The surface-area-based Generalized Born model[44] with an implicit solvation model [45] was used (VSGB 2.0) in the calculations. The OPLS3 force field employs a CM1A-BCC-based charge model based on a combination of the Cramer–Truhlar CM1A charges[46, 47] with an extensive parameterization of bond charge correction terms (BCC).

The default procedure consists of three simulations consisting of the receptor alone, ligand alone, and receptor-ligand complex. The original interaction terms include Coulombic, H-bond, GB solvation, van der Waals, p-p packing, self-contact, and lipophilic. The total binding free energy equation was then calculated via:

$$\Delta E_{bind} = E_{complex} - E_{ligand} - E_{receptor}$$

The interaction terms were then merged into three components, $E_{elctrostatics,}$ $E_{vdW,}$ and $E_{lipophilic}$, where:

$$E_{electrostatics} = H_{bond} + E_{coulomb} + E_{GB\_solvation}$$

$$E_{vdW} = E_{vdW} + E_{\pi\text{-}\pi} + E_{self\text{-}contact}$$

The MM-GBSA scoring function lacks the solute conformational entropy, which results in higher negative values when compared to the actual values. Nevertheless, when used to rank different drugs targeting receptors with comparable binding entropy values, it has proven to be an effective approximation[44].

Density functional theory simulations. To gain insights into the nature of the H-bonding and dispersion interactions between pimodivir and the residues in the active site, we performed energy decomposition analyses (EDA) on truncated small models representative of the interactions in the active site. The geometries of the small models were fully optimized and confirmed to have all real harmonic frequencies at the B3LYP-D3BJ/6-31+G(d,p) level of theory[48, 49, 50, 51], where the protein-like environment in the active site was simulated by a homogeneous polarizable continuum model with the dielectric constant $\varepsilon = 4.0$[52, 53, 54]. The EDA calculations were performed using the second-generation ALMO-EDA scheme by Head-Gordon and co-workers[55]. The EDA calculations were performed with the ωB97M-V functional in conjunction with the Def2-SVPD basis set[56, 57]. The geometry optimizations were performed using the Gaussian 16 program suite[58] and the EDA calculations were performed using the Q-Chem program suite[59].

Dynamic Cross Correlation Matrix. To gain a further understanding of the overall stability of the protein-ligand complexes, a dynamic cross-correlation matrix (DCCM) was generated for each system using Carma[60]. The program Carma calculates covariance and pairwise correlations (Cij):

$$C_{ij} = \frac{\langle \Delta\vec{r}_i(t)\cdot\Delta\vec{r}_j(t)\rangle}{(\langle \Delta\vec{r}_i(t)^2\rangle\langle\ \Delta\vec{r}_j(t)^2\rangle)^{1/2}}$$

between pairs of atoms across and the MD trajectory. The extracted MD trajectory included 273 atoms, where 1-272 corresponds to the protein Cα atoms and 273 corresponds to the center 19 atom of the ligand, as shown in **Figure 8**. This trajectory of each system was used to calculate the covariance matrix which was then converted to the DCCM.

Results and Discussion

Ligand docking. First, we performed molecular docking simulations of Pimodivir incorporated into the PB2 in WT, Q306H, S324I, S324N, S324R, F404Y, and N510T systems. The 2D structure and docked conformation of Pimodivir in WT and mutant systems are similar, as depicted in **Figure 1**.

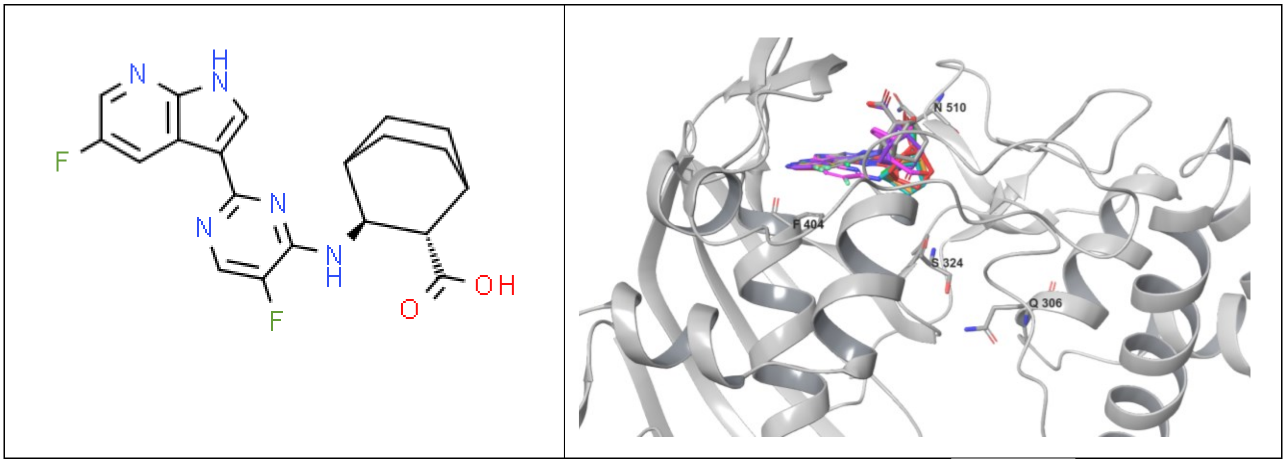

Figure 1. The 2D structure of Pimodivir (left) and docked poses of Pimodivir in WT (gray), Q306H (red), S324I (orange), S324N (green), S324R (blue), F404Y (purple), and N510T (pink) systems, with the positions of mutated residues.

Table 1 shows the binding energy predicted by XP-docking of Pimodivir in WT and mutant systems. The binding energies predicted by XP-docking are −9.3 kcal/mol, −6.6 kcal/mol, −7.0, −6.8, −7.0, −8.6, and −6.9 kcal/mol, for the WT, Q306H, S324I, S324N, S324R, F404Y, and N510T systems, respectively. These binding energies indicate that the mutation induces a reduced binding energy of Pimodivir to PB2 protein.

Table 1. The XP docking score of Pimodivir to Wildtype and mutant systems of polymerase basic protein 2 (PB2) (in kcal/mol).

No.	System	XP	ΔXP[a]
1.	WT	-9.3	
2.	Q306H	-6.6	2.7
3.	S324I	-7.0	2.3
4.	S324N	-6.8	2.5
5.	S324R	-7.0	2.3
6.	F404Y	-8.6	0.7
7.	N510T	-6.9	2.4

[a] Difference between the WT and mutant systems, a positive value indicates reduced binding energy.

Pimodivir interactions with PB2 in the WT system via five hydrogen bonds formed with the Arg332, Arg355, His357, and Glu361 residues. Figure 2 shows a truncated model of pimodivir in the active site taken from the docking simulations. The Arg355 residue interacts with the carboxylate group of pimodivir via two H-bonds, and the His357 residue interacts with the carboxylate group via one H-bond. The carboxylate group of the Glu361 residue interacts with the pyrrole ring of pimodivir via one H-bond, and the Arg332 residue interacts with the pyridine nitrogen via one H-bond (Figure 2). Density functional theory calculations can provide insights into the noncovalent interactions involved in the above H-bonds. For this purpose, we performed energy decomposition analyses (EDA) using the full structure of pimodivir and the H-bond donating or accepting moiety of each of the residues, namely guanidinium cation (for Arg332 and Arg355), acetate anion (for Glu361), and imidazole (for His357). These complexes were fully optimized at the B3LYP-D3BJ/6-31+G(d,p) level of theory, where the protein-like environment in the active site was simulated by a homogeneous polarizable continuum model with the dielectric constant $\varepsilon = 4.0$. The EDA calculations were performed using the second-generation ALMO-EDA scheme. With the exception of the Arg355•••pimodivir complex, all the complexes provide a good representation of the H-bonding and dispersion interactions found in the full system (see Table S1 of the Supporting Information).

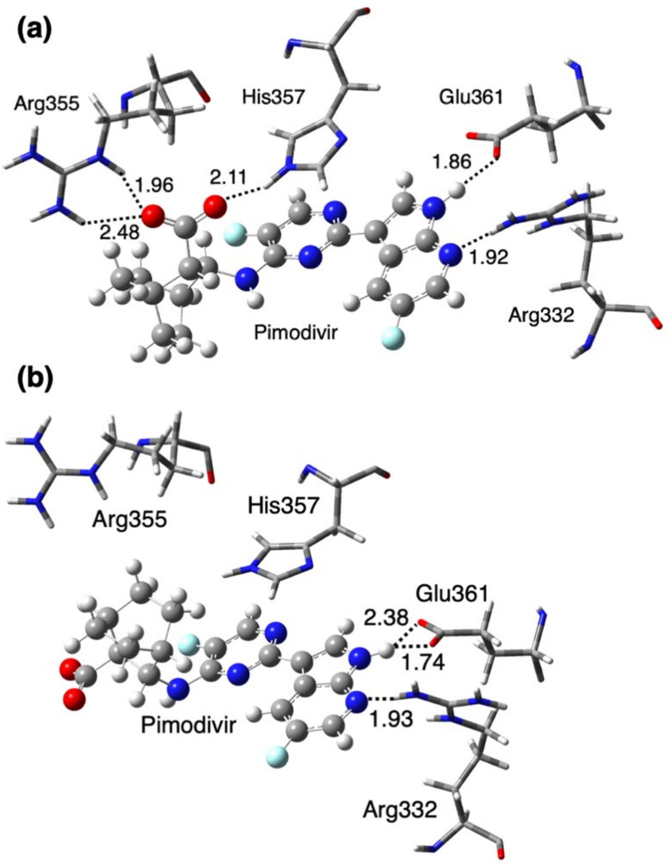

Figure 2. Truncated model of pimodivir in the active site of (a) the wildtype polymerase basic protein 2 (PB2) and (b) the N510T mutant. The hydrogen bonds between pimodivir and the Arg355, His357, Glu361, and Arg332 residues are shown as dotted lines and the H-bond lengths are given in Å. The structures are taken from the docking simulations.

The EDA calculations reveal that the dispersion energy component results in stabilizing interactions of -5.3 (Arg332), -5.0 (Glu361), and -10.2 (His357) kcal/mol. As expected, the dispersion interaction in His357•••pimodivir is much stronger than for the other residues, reflecting the p-stacking interactions between the aromatic rings of His357 and pimodivir (Figure 2a). Polarization interactions are rather significant for the H-bonds between pimodivir and the charged residues Arg332 and Glu361, namely, they amount to -11.1 and -13.5 kcal/mol, respectively. However, for the neutral His357 residue they amount to merely -4.1 kcal/mol. Likewise, charge-transfer interactions are 4–5 times as large for the charged Arg332 and Glu361 residues compared to those in the neutral His357 residue. Namely, they are -4.5 (Arg332), -5.5

(Glu361), -1.1 (His357) kcal/mol. The stronger polarization and charge-transfer interactions between pimodivir and the charged Arg332 and Glu361 residues are reflected in shorter H-bond distances of 1.92 and 1.86 Å, respectively, in the full system, compared to a longer H-bond distance of 2.11 Å obtained for the His357 residue (Figure 2a). The qualitative agreement between our truncated models and the full system increases our confidence in the above EDA results.

It is of interest to compare the EDA results for the WT system with those obtained for the key N510T mutant system. Figure 2b shows the H-bonds involved in both structures. Two key differences between the two structures are that the H-bonds between the carboxylate group of pimodivir and the Arg355 and His357 residues, which are present in the WT system, are not present in the N510T mutant system. Instead, in the N510T mutant system, the Arg355 and His357 residues interact with pimodivir via weaker dispersion interactions. This is illustrated in our EDA calculations by reduced polarization and charge-transfer interactions between pimodivir and the His357 residue. Namely the polarization interactions are -4.1 (WT) and -2.2 (N510T) kcal/mol, and the charge-transfer interactions are -1.1 (WT) and -0.5 (N510T) kcal/mol. For the Arg355 our small models calculations are not representative of interactions in the full system, however, due to the absence of H-bonding interactions in the N510T mutant, we expect that similar observations will hold for the polarization and charge-transfer interactions between pimodivir and the Arg355 residue.

In the mutant systems Q306H, S324I, S324N, and S324R these H-bonding interactions are altered in the mutant systems. Namely, three H-bonds that are observed in WT system with Arg332, Arg355, and His357 disappear, and a new H-bond with Val511 forms in the Q306H system, while those with Lys376 and Val511 were observed in S324I, S324N and S324R systems. In the F404Y H-bond with Arg332 disappeared, while in the N510T system, H-bonds with Arg355 and His357 disappeared without any new H-bond formed.

Furthermore, p-p stacking interactions observed in WT system were Phe323, Arg332, His357, and Phe363. In the Q306H, S324I, S324N, and S324R, one p-p stacking interactions with Arg332 was disappeared. However, in those four mutants, new p-p interactions with Phe404 were formed. In the F404Y system three p-p stacking interactions with Phe323, Arg332, and

Phe363 disappeared with additional p-p staking formed with Tyr404. However, N510T system preseverd all the p-p stacking interaction observed in WT system in addition new interaction with Phe404. The 2D interactions of WT and N510T systems was shown in **Figure 3**, while those for other systems were shown in **Figure S1**.

A. WT system

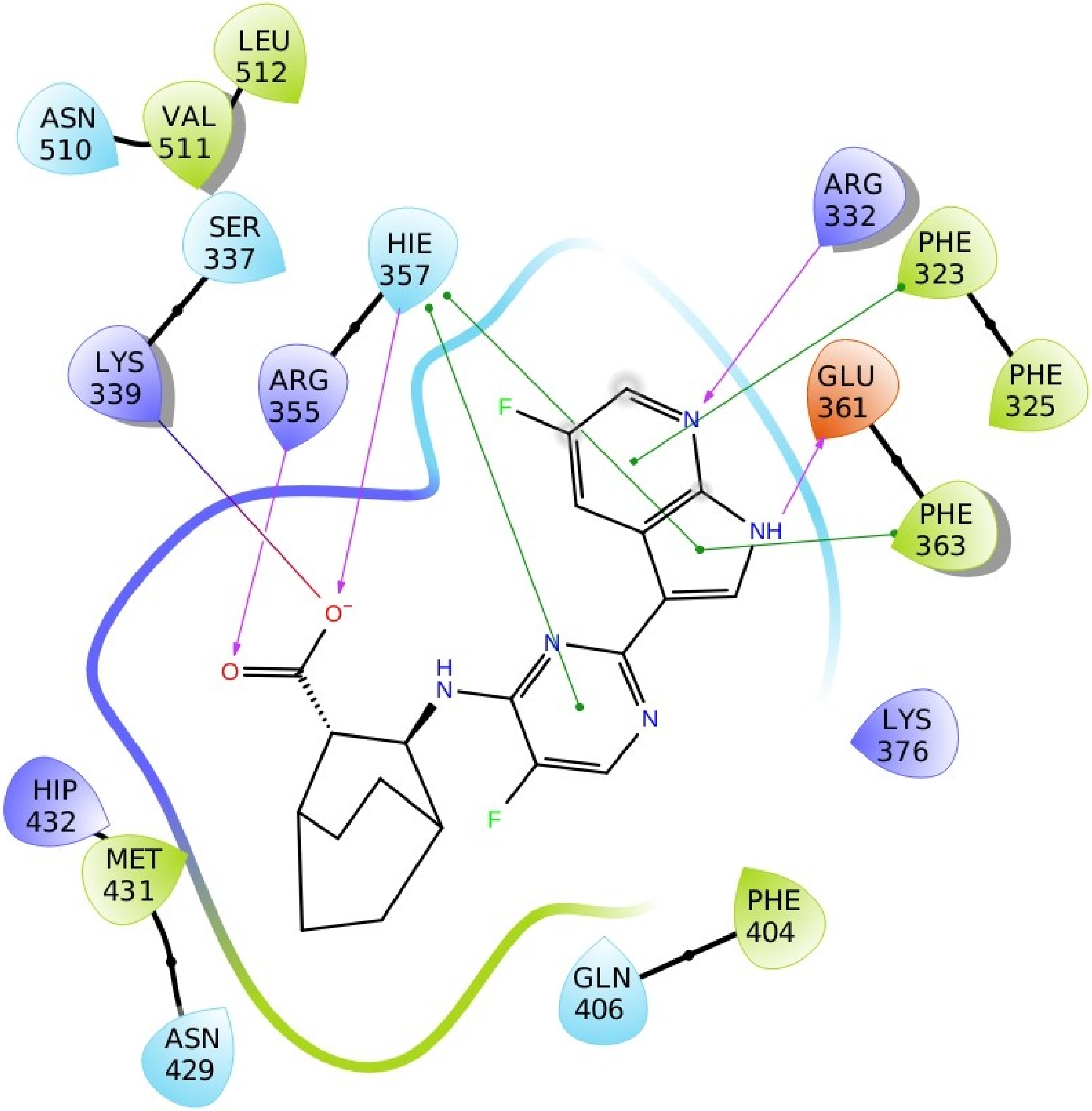

B. N510T system

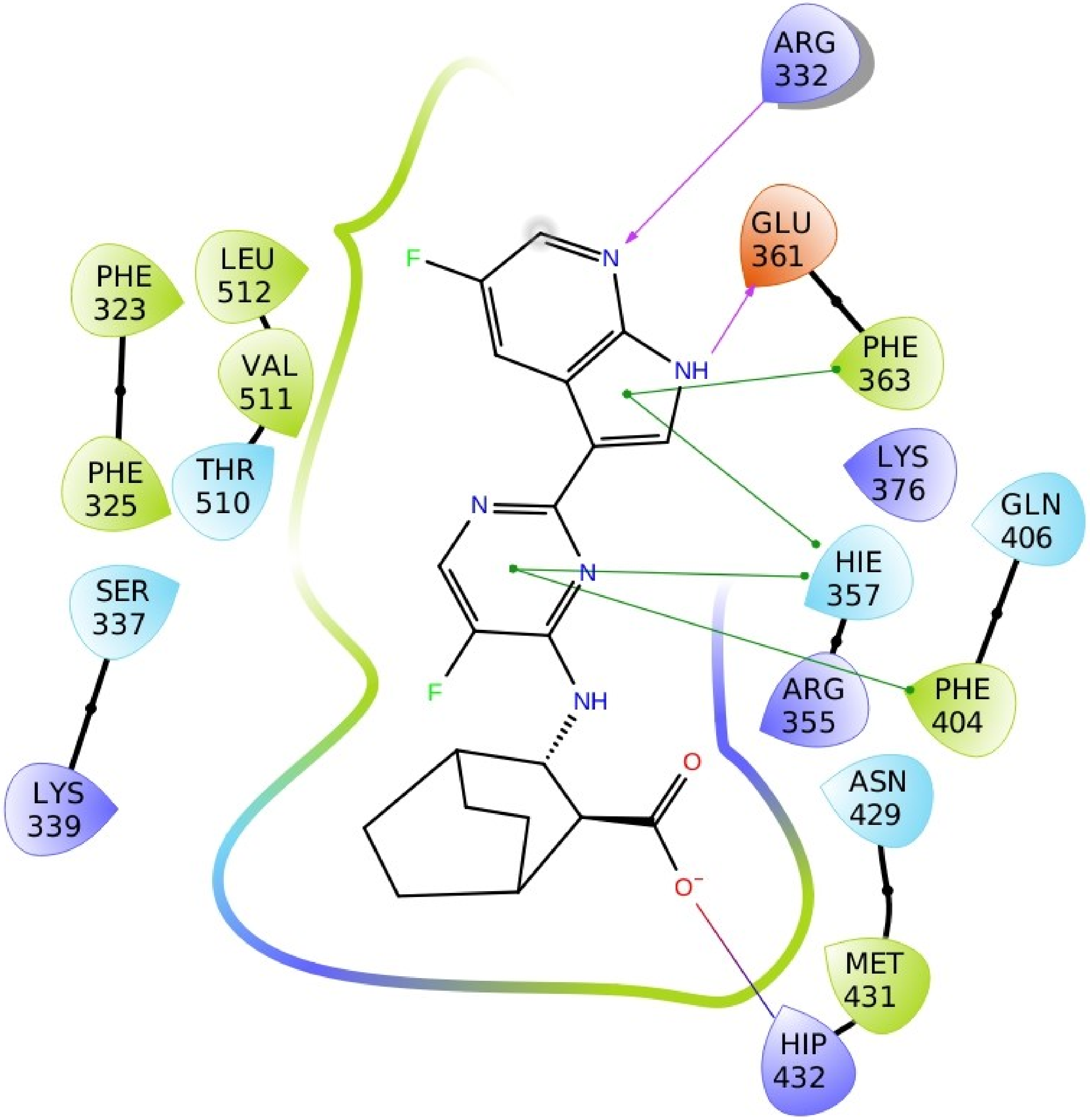

Figure 3. The 2D interaction of Pimodivir in WT **(A)** and N510T **(B)** systems.

RMSD values. The RMSD of protein Cα and Pimodivir of each system during 100 ns is depicted in **Figure 4.** The alpha carbons (Cα) of the protein is all systems were kept steady throughout 100 ns. It shows that the protein Cα was relatively more stable in WT (mean values of 1.82 Å), compared to those in Q306H (2.05 Å), S324I (2.26 Å), S324R (2.53 Å), F404Y (1.87 Å), and N510T (2.07 Å), but it was higher than that in S324N (1.49 Å).

Table 2. The mean RMSD of Protein Cα atoms and Mean RMSD of ligand calculated for Wild type (WT) and mutant systems.

System	Mean RMSD of Protein Cα atoms (Å)	Mean RMSD of ligand (Å)
WT	1.82 ± 0.31	2.01 ± 0.53
Q306H	2.05 ± 0.37	1.37 ± 0.23
S324I	2.26 ± 0.43	1.66 ± 0.35
S324N	1.49 ± 0.22	1.04 ± 0.27
S324R	2.53 ± 0.38	1.02 ± 0.23
F404Y	1.87 ± 0.24	0.93 ± 0.23
N510T	2.07 ± 0.29	3.71 ± 1.62

However, Pimodivir had a more fluctuant RMSD in WT (2.01 Å) compared to those in Q306H (1.37 Å), S324I (1.66 Å), S324N (1.04 Å), S324R (1.02 Å), F404Y (0.93 Å) systems, but it was lower than that in N510T (3.7 Å). The Pimodivir is shown to have abrupt increase at about 60 ns when the phenyl ring of Pimodivir underwent a positional change, which indicated that the ligand in the N510T system were the most unstable during MDS. It is clear that the protein mutations have impacted the Pimodivir conformation to be more fluctuant in N510T system, but more stable in other mutant systems.

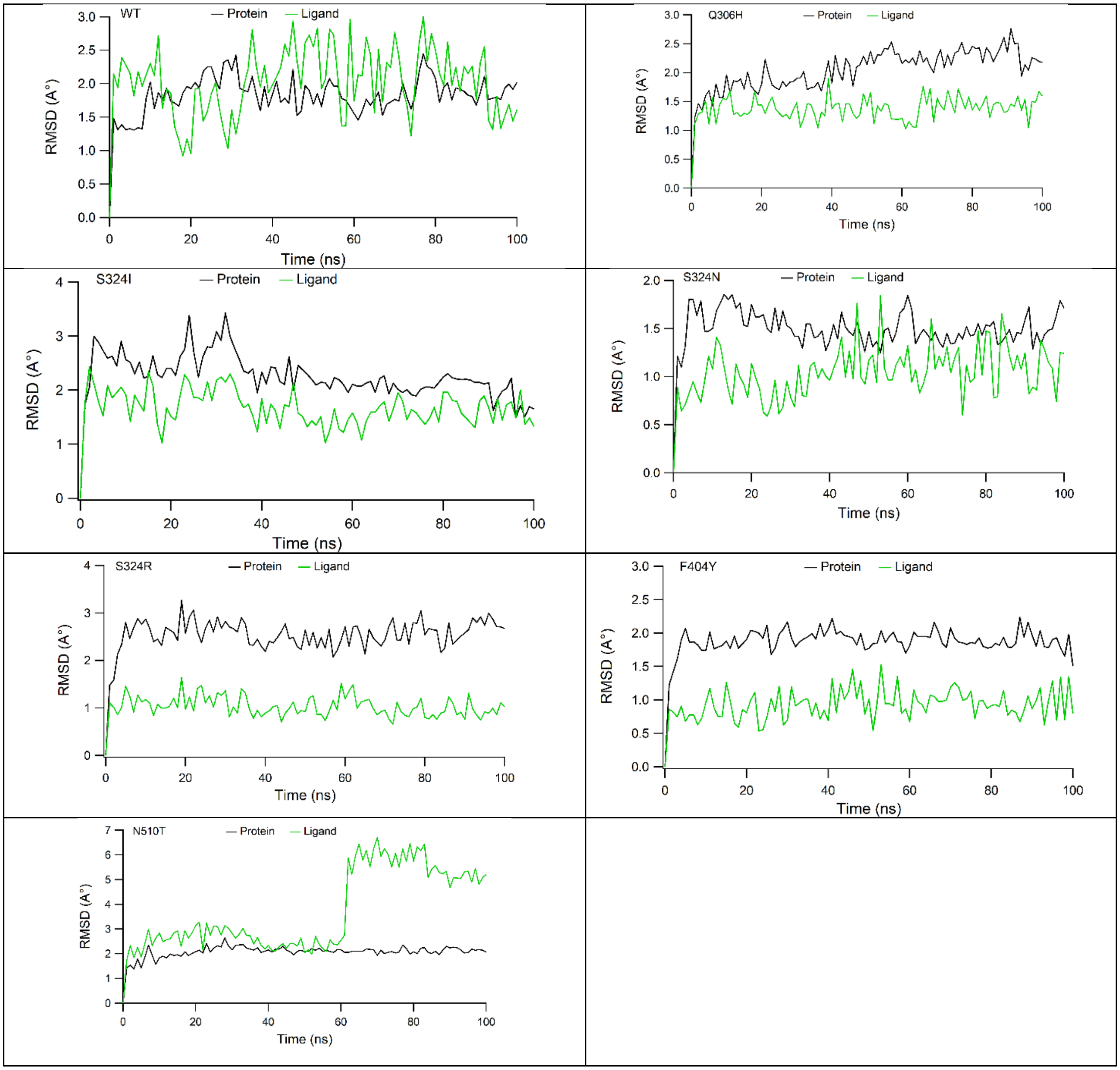

Figure 4. The root mean squared deviation (RMSD) of Protein Cα (black line) and ligand (green light) in WT, F404Y, N510T, S324I, S324N, S324R, and Q306H systems.

The Protein-Ligand Interaction Analysis. To acquire a protein-ligand interaction during MDS, analysis of the simulation interaction diagram (SID) was performed. Interaction fraction with corresponding residues and protein-ligand interactions which sustained more than 20% of MDS is depicted in Figure 5. In the WT system (Figure 5A), H-bond interactions were observed with Glu361 (80% occupancy), Arg355 (98% and 91% occupancies) and Arg332 (45% occupancy), in addition to p-p interaction with His357 (81% and 67% occupancies) and Phe323 (36% occupancy). The water-mediated H-bond was also seen with Phe404 (86% occupancy), which indicates their role to stabilize Pimodivir binding.

In the Q306H system (**Figure 5B**), H-bond interactions were observed with Glu361 (94% occupancy), Val511 (95% and 66% occupancies), and Lys376 (84% occupancy). The high occupancies of H-bonds with Glu361, Val511, and Lys376 were also seen in S324I (**Figure 5C**) (98%, 99% and 39%, and 87% occupancies), S324N (**Figure 5D**) (98%, 97%, 44% occupancies), S324R (**Figure 5E**) (98%, 100%, and 37% occupancies), and F404Y (**Figure 5F**) (94%, 95%, and 47% occupancies). However, the H-bond with Glu361 was much reduced in N510T system (**Figure 5G**) (55% occupancy), while those with Val511 and Lys376 were completely lost, and new H-bonds with Asn429 (79% occupancy) and His432 (80% occupancy) formed. The F404Y system particularly maintained additional high H-bond interactions with Arg355 with 96% and 90% occupancies.

In almost all mutant systems, the p-p interactions with Phe323 were observed with high occupancies (96% in Q306H, 86% in S324I, 85% in S324N, 81% in S324R, 81% in F404Y), however, it was lost in N510T system. The high occupancies of p-p interactions were also observed with Phe404/Tyr404 in Q306H, S324I, S324R, F404Y systems (each 80%, 77%, 69%, and 73%, respectively), but they became low in S324N and N510T (32% and 43% occupancies, respectively). The interactions with Phe363 were also high in Q306H (79% occupancy), but it reduced in S324N (60% occupancy), S324R (58% occupancy), F404Y (53% occupancy), and S324N (39% occupancy), and again it disappeared in N510T system. In addition, the S324I, S324N, S324R, F404Y systems maintained high occupancies of p-p interactions with His357 each with 87%, 79%, 87%, and 71%, respectively, but it reduced in Q306H and N510 systems (54% and 37% occupancies, respectively).

The water-mediated H-bond was variable among mutant systems, for example Q306H with Lys339 (51% occupancy), S324I system with Arg332 (45% occupancy), S324N with Lys339 (33% occupancy), S324R with Val511 (47% occupancy), F404Y with Arg332 (54% occupancy) and Met431 (33% occupancy), and N510T system with Val511 (47% occupancy). It was clear that while other mutant systems maintained interactions with key residues with high occupancies, the interactions has much reduced or lost in N510T system. **Figure 5 and S3** show **t**he 2D protein-ligand interaction diagrams lasting more than 20% of the MDS.

A. WT system

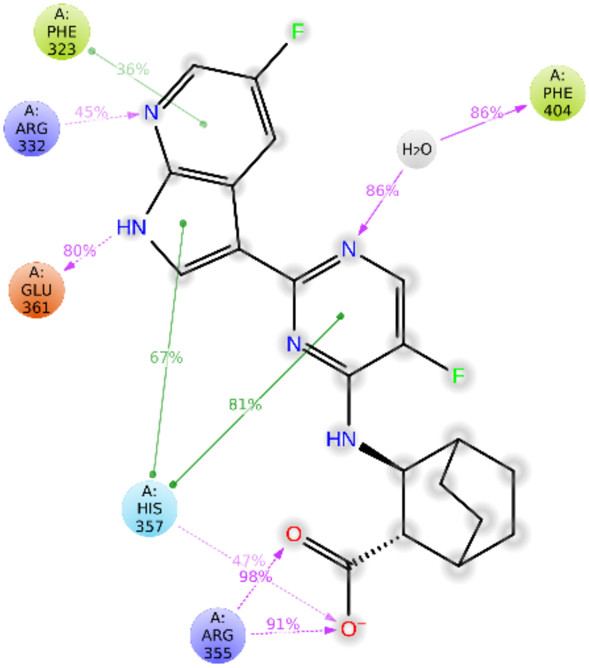

B. N510T system

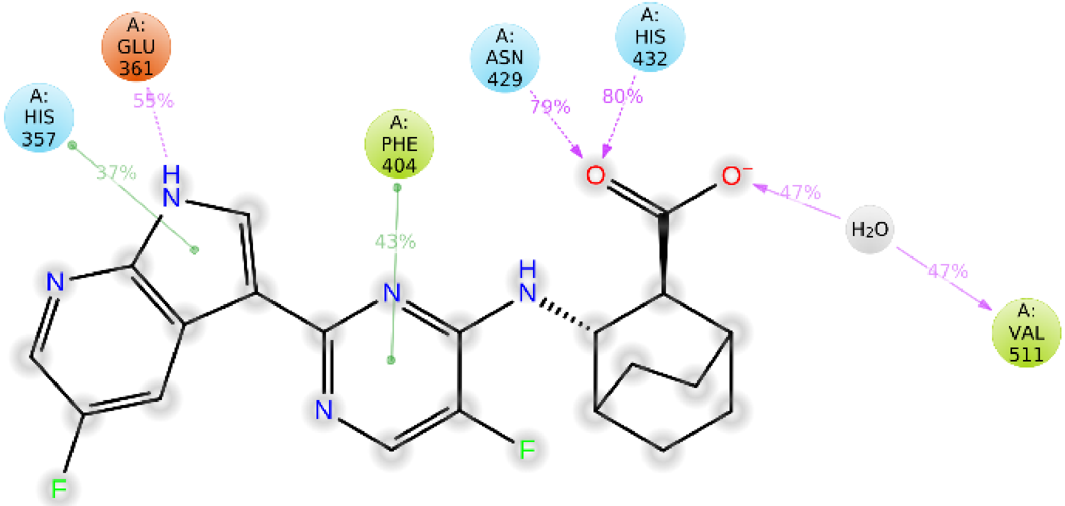

Figure 5. The 2D Protein-Ligand Interaction Diagrams lasting more than 20% of the MDS (**A:** WT-Pim; **B:** N510T-Pim) recorded during MD simulations.

Cluster analysis. To acquire the dominant conformations of the protein-ligand complex, we performed clustering analysis on each system and analyzed the ligand binding sites from best cluster. We found out that in the WT system (**Figure 6**), H-bond interactions were observed with Glu361, Arg355, and His357, in addition to p-p interaction with His357. The water-mediated H-bond was also seen with Lys339. H-bond with Glu361 and Val511 were observed in all mutant system except in N510T, while H-bonds with Lys376 were observed in S324I, S324N, and S324R systems. H-bond with Lys339 and Arg555 were observed S324N and F404Y, respectively. In addition, all mutant systems maintained p-p interactions with His357 except in N510T, while p-p interactions with Phe323 and Phe404/Tyr404 were observed in Q306H, S324I, S324R, and F404Y systems. F404Y and S324N maintained additional p-p interactions with Phe363, while in N510T system no p-p interaction was observed, but it formed new H-bonds with Arg508, His432, and Asn429. It is clear that the N510T mutation has changed much the interaction with crucial residues of the protein. **Figure 6** and **S4** show the active site conformation and 2D interactions of WT-Pim and mutant systems taken from most populated cluster.

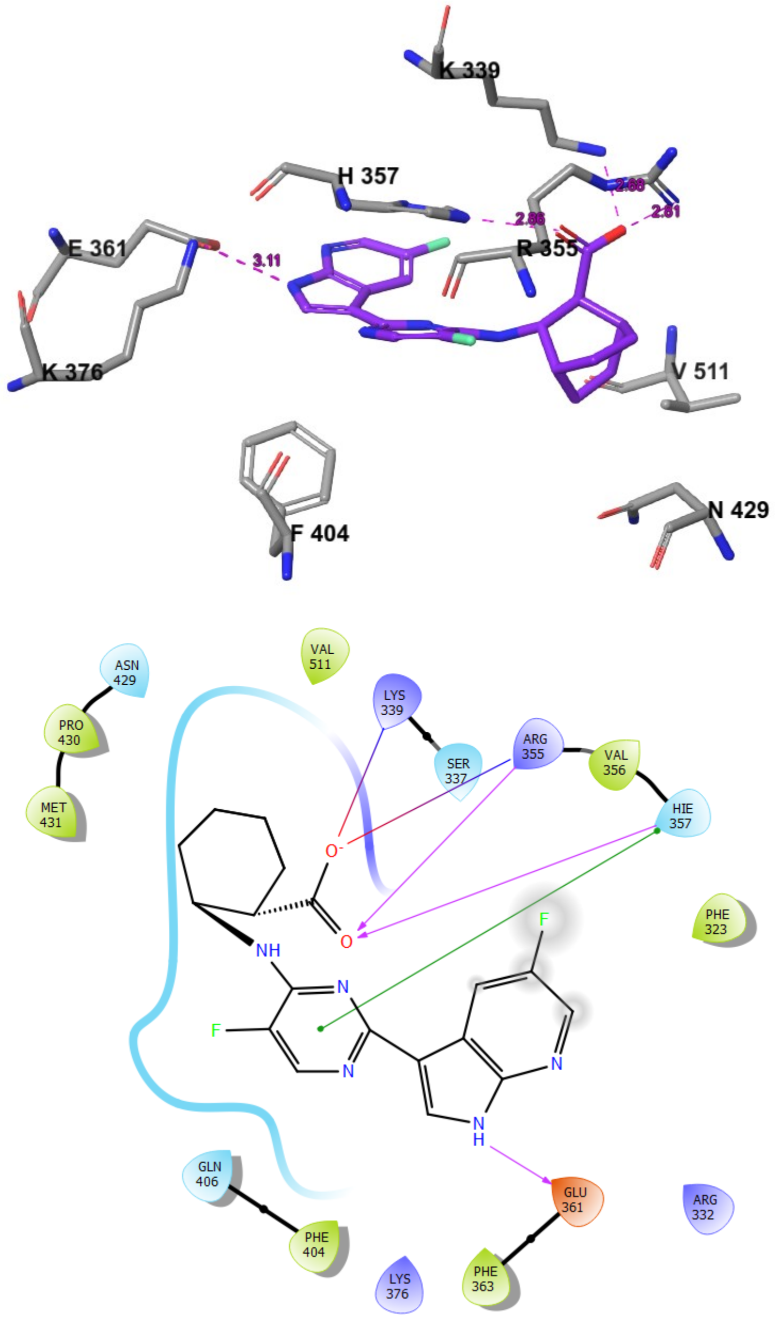

Figure 6. The active site conformation and 2D interactions of WT-Pim system taken from most populated cluster.

Binding energy prediction. The MM-GBSA binding energy was calculated to assess the effectiveness of the mutation on the binding energy of Pimodivir. The total binding energy for the WT system was −61.2 kcal/mol, which was lower than that in the N510T (−48.2 kcal/mol) and S324N (−60.4 kcal/mol) systems, but it was higher than those in the Q306H (−67.9 kcal/mol), S324I (−64.6 kcal/mol**)**, S324R (−65.3 kcal/mol), and F404Y (−65.2 kcal/mol). The binding energy changes between the WT system and those in the N510T, Q306H, S324I, S324N, S324R, and F404Y systems were 13 kcal/mol, 6.7 kcal/mol, 3.4 kcal/mol, 0.8 kcal/mol, 4.1 kcal/mol, and 4.0 kcal/mol, respectively. Clearly, among those mutations, N510T mutation resulted in much lower affinity of Pimodivir followed by S324N system, but a mutation in Q306H, S324I, S324R, and F404Y resulted in a slightly stronger affinity of Pimodivir. Table 3 shows the binding energy calculated for last 50 ns of each system.

Table 3. The binding energies (Δ*G*, kcal/mol) calculated for the last 50 ns of each trajectory.

Systems	**WT**	**Q306H**	**S324I**	**S324N**	**S324R**	**F404Y**	**N510T**
ΔG_{bind}	−61.2±4.7	−67.9±6.1	−64.6±4.2	−60.4±4.4	−65.3±4.4	−65.2±6.4	−48.2±7.8
$\Delta\Delta G_{\mathrm{bind}}$		−6.7	−3.4	0.8	−4.1	−4.0	13.0
ΔE_{vdw}	−42.9±3.9	−59.9±4.2	−57.9±3.4	−51.8±3.9	−57.6±3.7	−51.4±4.7	−40.3±7.3
$\Delta\Delta E_{\mathrm{vdw}}$		17.0	15.0	8.9	14.7	8.5	2.6
ΔE_{ele}	−3.0±4.3	11.5±3.2	12.9±2.3	10.1±4.1	11.9±2.9	5.1±4.3	5.4±4.0
$\Delta\Delta E_{\mathrm{ele}}$		14.5	15.9	13.1	14.9	8.1	8.4
ΔE_{lipo}	−15.3±1.5	−19.5±1.4	−19.6±1.1	−18.7±1.1	−19.7±0.9	−18.9±1.2	−13.4±2.3
$\Delta\Delta E_{\mathrm{lipo}}$		4.2	4.3	3.4	4.4	3.6	1.9

It was observed that the van der Waals interactions (ΔE_{vdw}) is the dominant factor when considering favorable binding contributions, each with −42.9 kcal/mol, −59.9 kcal/mol, −57.9 kcal/mol, −51.8 kcal/mol, −57.6 kcal/mol, −51.4 kcal/mol, and −40.3 kcal/mol in WT, Q306H, S324I, S324N, S324R, F404Y, and N510T, respectively. The differences of van der Waals interactions ($\Delta\Delta E_{\mathrm{vdw}}$) were 17 kcal/mol, 15 kcal/mol, 8.9 kcal/mol, 14.7 kcal/mol, 8.5 kcal/mol, and 2.6 kcal/mol in Q306H, S324I, S324N, S324R, F404Y, and N510T systems, each compared to the WT system.

Meanwhile, the lipophilic interactions (ΔE_{lipo}) were also more positive in the N510T system (−13.4 kcal/mol) than in other systems each with −15.3 kcal/mol, −19.5 kcal/mol, −19.6 kcal/mol, −18.7 kcal/mol, −19.7 kcal/mol, −18.9 kcal/mol in WT, Q306H, S324I, S324N, S324R, and F404Y, respectively. The mutations have reduced the van der Waals and lipophilic interactions in N510T system with 2.6 kcal/mol and 1.9 kcal/mol changes compared to the WT system, respectively.

It was clear that the van der Waals energy were more positive in the N510T system compared to other systems. The possible explanations are the H-bond decreased percentage with Glu361 and disappearance of H-bonds with Val511 in the T179A system (Figure 4B).

It was observed that the electrostatic energy (ΔE_{ele}) is favorable binding contributions to WT with −3.0 kcal/mol, however it became unfavorauble in Q306H, S324I, S324n, S324R, F404Y, and N510T systems each with 11.5 kcal/mol, 12.9 kcal/mol, 10.1 kcal/mol, 11.9 kcal/mol, 51.1 kcal/mol, and 5.4 kcal/mol, respectively. The differences of electrostatic interactions ($\Delta\Delta E_{\mathrm{ele}}$) were 14.5 kcal/mol, 15.9 kcal/mol, 13.1 kcal/mol, 14.9 kcal/mol, 8.1 kcal/mol and 8.4 kcal/mol in Q306H, S324I, S324n, S324R, F404Y, and N510T systems, respectively, each compared to the WT system.

The RMSF values. The RMSF of protein Cα atoms were compared between protein WT and the mutants. Each prominent RMSF value was assigned with black, red, orange, green, blue, purple, pink arrows in WT, Q306H, S324I, S324N, S324R, F404Y, and N510T systems, respectively (**Figure 7**). The highest peaks are residues of carboxyl and amino ends of the protein. The high peaks at N456, G459, and Y488, were a protein loop, while the key residues intecating with protein were observed stable. Concisely, mutation in N510T induced the largest impact on protein residues compared to other mutations.

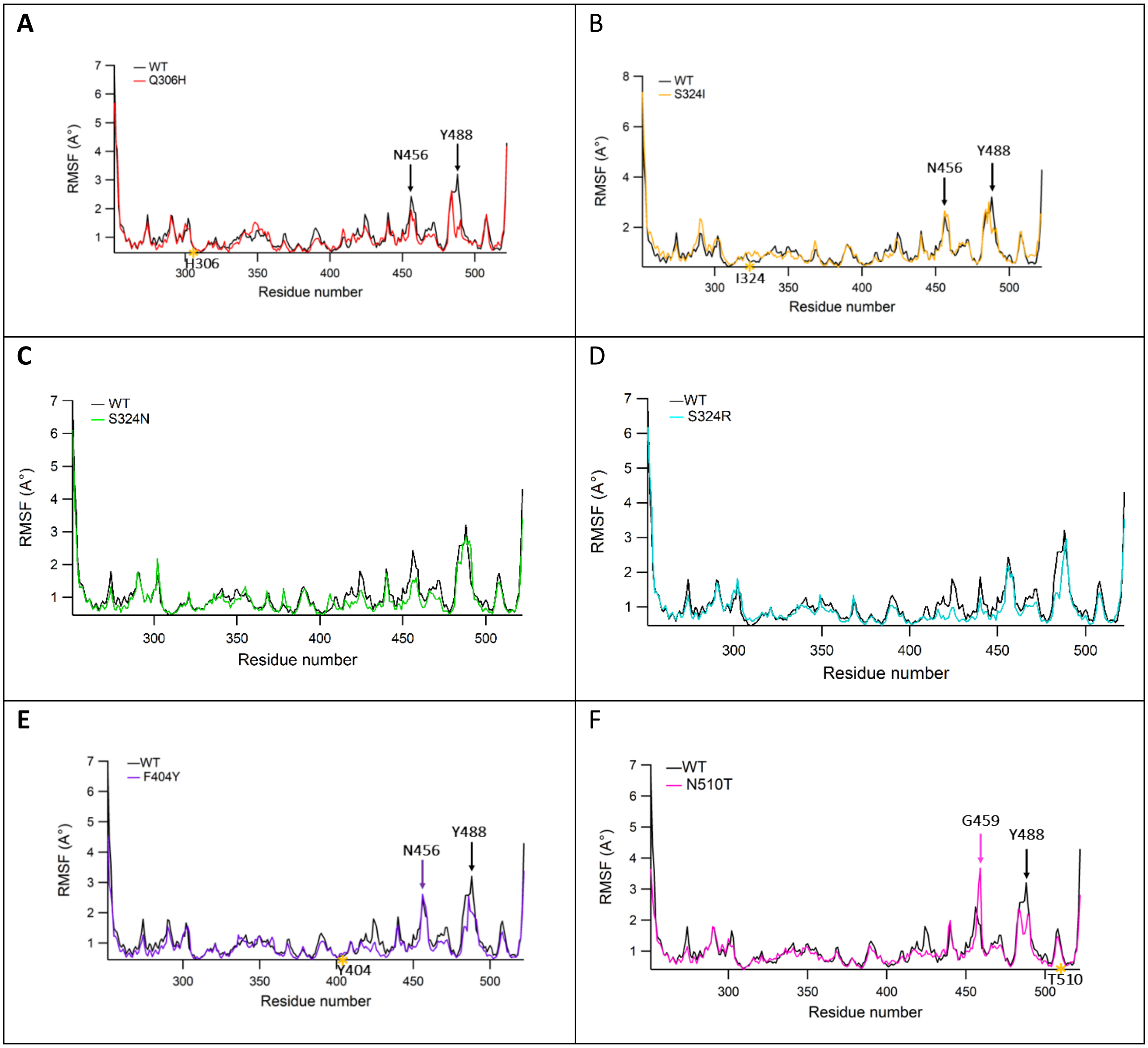

Figure 7. The RMSF values comparison between WT and Q306H (A), WT and S324I (B), WT and S324N (C), WT and S324R (D), WT and F4-4Y (E), and WT and N510T (F). The RMSF values of the C_α atoms for residues in WT (black), Q306H (red), S324I (orange), S324N (blue), S324R (blue), F404Y (purple), and N510T (pink) are shown with the mutant positions are noted by yellow asterisks.

Ligand RMSF Values. The RMSF values of the ligand atoms were recorded as depicted in **Figure 8**. A higher fluctuation of ligand generally reflect its lower stability in the protein binding site. The RMSF of Pimodivir in WT system was lower with mean RMSF values (1.51 Å) compared to those in N510T (2.39 Å), but it was higher than those in Q306H (0.69 Å), S324I (0.85 Å), S324N (0.88 Å), S324R (0.68 Å), and F404Y (0.70 Å) systems, which indicated that Pimodivir was more stable in the WT system than in N510T but it was less stable compared to in Q306H, S324I, S324N, S324R, and F404Y systems. It is showed that the most fluctuant atoms in N510T were those in the the phenyl ring (atom number 9) as shown by their highest peaks .

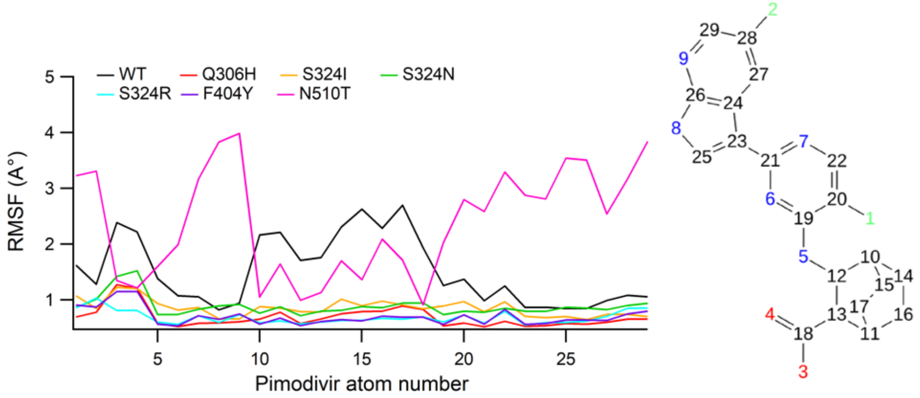

Figure 8. The RMSF values for atoms of Pimodivir.

The secondary structure of the protein. The SSE of protein monitored during MDS were plotted in **Figure 9**, which displays the distribution of SSE, including Alpha-helices and Beta-strands by residue. The total percentage of SSE for WT, Q306H, S324I, S324N, S324R, F404Y, and N510T were 51.96%, 50.82%, 51.42%, 51.22%, 52.12%, 50.85%, and 48.67%, respectively. It was clear that the mutation in N510T system has reduced the SSE percentage in the system, but the mutation in the other system had minor effects on SSE of the protein.

	WT system	**N510T system**
Ligand torsion	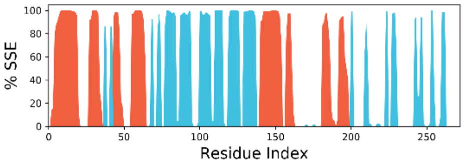	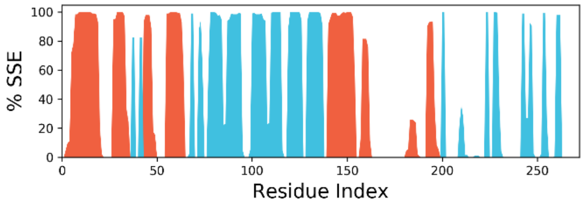
	Q306H system	**S324I**
Ligand torsion	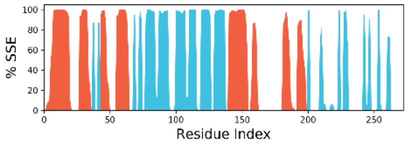	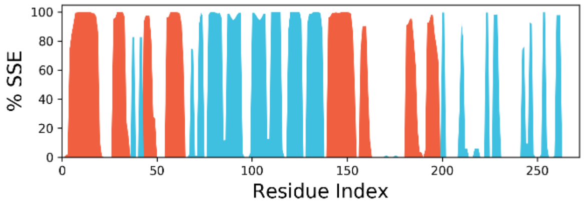
	S324N system	**S324R system**
Ligand torsion angles	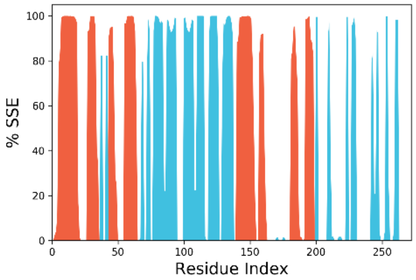	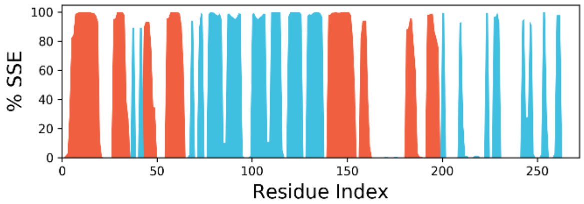
	F404Y system	
Ligand torsion	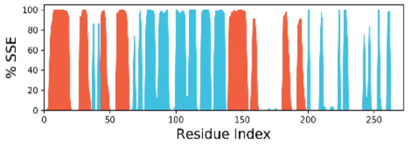	

Figure 9. Protein SSE for the WT, Q306H, S324I, S324N, S324R, F404Y, and N510T systems during MDS. The alpha helices, beta sheets, and random coil were represented by red, blue, and white spaces.

Dynamic Cross-Correlation Matrix Analysis. The single-point mutation N510T rather than the Q306H, S324I, S324N, S324R and F404Y single-point mutations induces a very different dynamic response in the ligand-binding region that is far from the mutation site, as shown in the dynamic cross-correlation matrix (DCCM) (**Figure 10**). The DCCM of the seven systems were calculated by the Carma program, as described in the methods section. A pairwise comparison of the DCCMs from all six mutant systems are included in the supporting document **(Figures S6-S11)**. The dynamical structure of the systems can be further elucidated upon viewing the topology diagram **(Figure S5)**. In both the N-terminal and ligand-binding domain, as seen in **Figure 10**, there appears to be perpendicular signals to the diagonal. As shown in **Figure S5**, this is due to the strong hydrogen bonds coupling the long-distance alpha helices and beta sheets. The DCCM for the WT and N510T systems generated in **Figure 10** displays subtle differences in the dynamical structure of the protein. Notably, the ligand-binding domain region appears to be more yellow (+0.5) in the N510T mutant system than the WT system, which appeared redder (+1). Overall, it was clear that the single-point mutation in the N510T system has reduced positive correlation, but the mutations in the other five mutant systems were comparable with the WT system.

WT system	**N510T system**
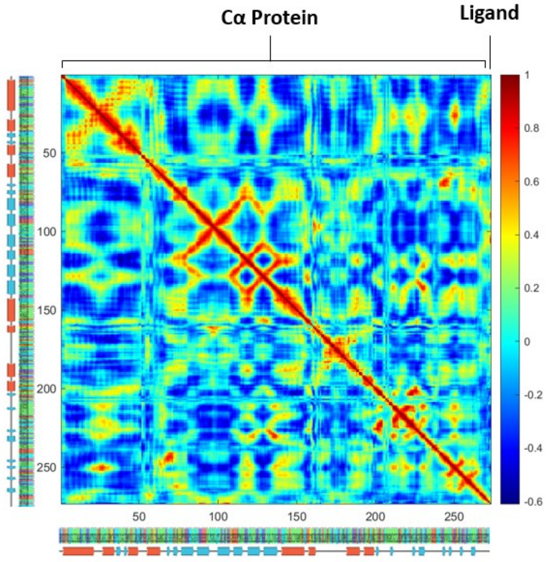	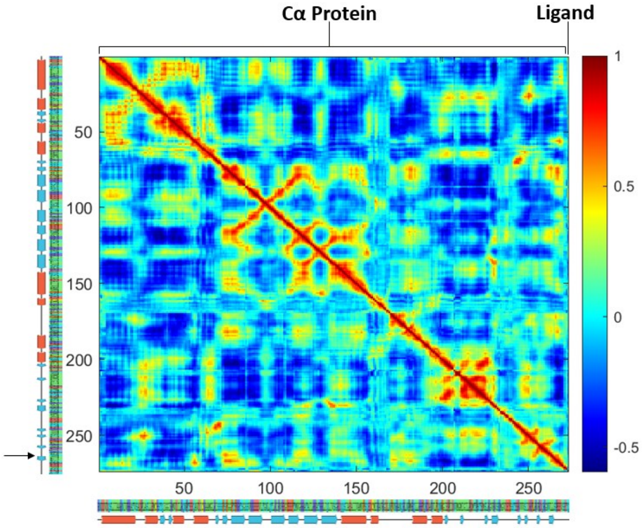

Figure 10. Dynamic cross-correlation matrix (DCCM) for the WT and N510T systems. 1-272: protein Cα atoms. 273: the center atom (19 of Fig. 8) of the ligand. 1-272 corresponds to 251-675 in the full sequence. The sequence and the secondary structure of the protein is provided along the x and y axes.

Correlation Coefficient Plot. To understand the dynamic change of the protein-ligand complexes due to a single-point mutation, the correlation coefficients between the ligand center atom (19 of **Fig. 8**) position and the protein residue CA position (1-272) were extracted from the DCCM and plotted in **Figure S12**. The differences between the six single-point mutants and WT are shown in **Figure 11**, which was divided into three regions. Region 1 corresponds to the N-terminal, where it is shown that the N510T system has a significantly higher positive correlation than the other five mutant-Q306H, S324I, S324N, S324R, and F404Y-systems. In region 2, which corresponds to the ligand-binding domain, we see that the N510T system shows a negative correlation response in comparison to the five other single-point mutants, which show a positive correlation. Region 3, corresponding to the N510T mutation region, additionally exhibits an opposite, negative correlation in the N510T system in comparison to the other mutant sytems. In **Figure 11**, seven key residue interactions, which were present in more than four systems **(Table S2)**, are indicated by a black arrow. The red arrows indicate the the six single-point mutations. Ultimately, this demonstrates the allosteric effects, explaining why the N510T single-point mutation had a significantly reduced binding energy in the MMGBSA analysis **(Table 3)**.

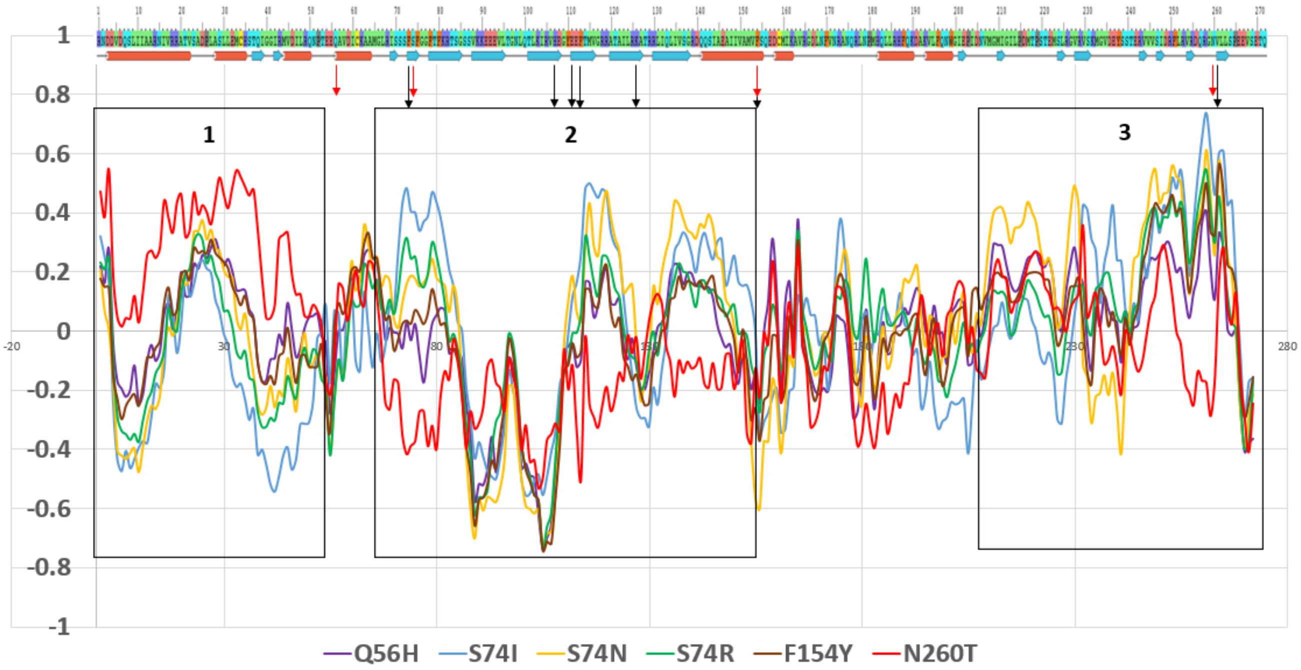

Figure 11. The changes of correlation coefficients between the ligand center atom (19 of Fig. 8) position and the protein residue Cα position upon a single-point mutation in the WT system. Single point mutations include Q306H, S324I, S324N, S324R, F404Y, and N510T, which corresponds to Q56H, S74I, S74N, S74R, F154Y, and N260T, respectively. Black arrows indicate key residue interactions occuring within the six systems. Red arrows indicate mutated residues. The sequence and the secondary structure of the protein is provided along the top of the graph. Region 1 corresponds to the N-terminal region. Region 2 corresponds to the ligand-binding domain. Region 3 corresponds to the N510T single-point mutation region. The raw data for each system is included in Figure S12.

Conclusions

This study uses homology modeling, molecular docking, molecular dynamics, and density functional theory simulations, and dynamic cross-correlaton matrixes to provide a detailed understanding of the structural and chemical interactions governing the binding of Pimodivir to the IAV PB2 in the WT and mutant systems. We find that the key residues interacting with Pimodivir include Glu361, Arg355, Arg332, His35, and Phe323, which is consistent with the experimental results. Importantly, we show that the binding of Pimodivir in the mutant systems results in conformational changes of Pimodivir, which in turn results in a significantly reduced binding affinity in the N510T system. However, the effect of mutations in the other mutant systems was not found to be significant. In the N510T system, the low binding affinity is attributed to the absence of H-bonding interactions with the Arg355 and His357 residues, in addition to generally weaker van der Waals interaction. Analysis of the dynamic cross-correlation matrixes also appears to suggest that the mutant N510T induces a long-range allosteric effect in reducing the binding interaction. The present study reveals the molecular details of how a single mutation in PB2 of IAV affects the binding affinity of Pimodivir, which need further experimental validation. We hope that these results will be useful for the design of new improved analogues of Pimodivir with better binding affinities.

Supplementary Materials. Cartesian coordinates for the truncated models considered in the DFT/EDA calculations (Table S1). Ligand and protein residue contacts occurring within the WT and mutant systems. Mutant systems include the single-point mutations: S324I, S324N, S324R, Q306H, N510T, and F404Y. Residues highlighted in yellow indicate that more than four systems presented with this key residue interaction (Table S2). 2D interaction of Pimodivir in the mutant systems (Figure S1); The root mean squared deviation (RMSD) of Protein Cα (black line) and ligand (green light) in WT, in which the equilibration time was 1000 ps (Figure S2); 2D Protein-Ligand Interaction Diagrams lasting more than 20% of the MDS (A: Q306H-Pim; B: S324I-Pim; C: S324N-Pim; D: S324R-Pim; E: F404Y-Pim) recorded during MD simulations (Figure S3); The active site conformation and 2D interactions of Q306H-Pim (A), S324I-Pim (B), S324N-Pim (C), S324R-Pim (D), F404Y-Pim (E), N510T-Pim (F) systems taken from the most populated cluster (Figure S4); Topology diagram for PDB ID: 5FMM gathered from the PDBsum website. Red cylinders represent the α-helices. Pink arrows represent the β-sheets. Portions boxed in blue are regions outside the residues of interest: 1-272 protein Cα atoms. 1-272 corresponds to 251-675 in the full sequence (**Figure S5**); Dynamic cross-correlation matrix (DCCM) for the WT and Q306H systems. 1-272: protein Cα atoms. 273: the center atom (19 of Fig. 8) of the ligand.

1-272 corresponds to 251-675 in the full sequence. The sequence and the secondary structure of the protein is provided along the x and y axes. The black arrow along the y-axis indicates the location of single-point mutation Q306H (**Figure S6**); Dynamic cross-correlation matrix (DCCM) for the WT and S324I systems. 1-272: protein Cα atoms. 273: the center atom (19 of Fig. 8) of the ligand. 1-272 corresponds to 251-675 in the full sequence. The sequence and the secondary structure of the protein is provided along the x and y axes. The black arrow along the y-axis indicates the location of single-point mutation S324I (**Figure S7**); Dynamic cross-correlation matrix (DCCM) for the WT and S324N systems. 1-272: protein Cα atoms. 273: the center atom (19 of Fig. 8) of the ligand. 1-272 corresponds to 251-675 in the full sequence. The sequence and the secondary structure of the protein is provided along the x and y axes. The black arrow along the y-axis indicates the location of single-point mutation S324N (**Figure S8**); Dynamic cross-correlation matrix (DCCM) for the WT and S324R systems. 1-272: protein Cα atoms. 273: the center atom (19 of Fig. 8) of the ligand. 1-272 corresponds to 251-675 in the full sequence. The sequence and the secondary structure of the protein is provided along the x and y axes. The black arrow along the y-axis indicates the location of single-point mutation S324R (**Figure S9**); Dynamic cross-correlation matrix (DCCM) for the WT and F404Y systems. 1-272: protein Cα atoms. 273: the center atom (19 of Fig. 8) of the ligand. 1-272 corresponds to 251-675 in the full sequence. The sequence and the secondary structure of the protein is provided along the x and y axes. The black arrow along the y-axis indicates the location of single-point mutation F404Y (**Figure S10**); Dynamic cross-correlation matrix (DCCM) for the WT and N510T systems. 1-272: protein Cα atoms. 273: the center atom (19 of Fig. 8) of the ligand. 1-272 corresponds to 251-675 in the full sequence. The sequence and the secondary structure of the protein is provided along the x and y axes. The black arrow along the y-axis indicates the location of single-point mutation N510T (**Figure S11**); The correlation coefficients between the ligand center atom (19 of Fig. 8) position and the protein residue Cα position in the WT and single mutant systems. Black arrows indicate key residue interactions occuring within the seven systems. Single-point mutations include Q306H, S324I, S324N, S324R, F404Y, and N510T, which corresponds to Q56H, S74I, S74N, S74R, F154Y, and N260T, respectively. Red arrows indicate mutated residues. The sequence and the secondary structure of the protein is provided along the top of the graph. Region 1 corresponds to the N-terminal region. Region 2 corresponds to the ligand-binding domain. Region 3 corresponds to the N510T single-point mutation region (**Figure S12)**.

Data Availability Statement. The data supporting this study's findings are available within the article and its supplementary material and from the corresponding authors upon reasonable request.

Acknowledgments. MA would like to thank the Ministry of Education, Culture, Research, and Technology, Republic of Indonesia, for supporting the research through the Program World Class Professor (WCP) 2022. C.W acknowledges the support by the New Jersey Health

Foundation (PC 76-21) and the U.S. National Science Foundation under Grants NSF ACI-1429467/RUI-1904797, and XSEDE MCB 170088.

Conflicts of Interest: The authors declare no conflict of interest. The funders had no role in the design of the study, in the collection, analyses, or interpretation of data, in the writing of the manuscript, or in the decision to publish the results.

References

1. Iuliano AD, Roguski KM, Chang HH, et al. Estimates of global seasonal influenza-associated respiratory mortality: a modelling study. The Lancet. 2018;391(10127):1285-1300. doi: 10.1016/S0140-6736(17)33293-2.
2. Byrn RA, Jones SM, Bennett HB, et al. Preclinical activity of VX-787, a first-in-class, orally bioavailable inhibitor of the influenza virus polymerase PB2 subunit. Antimicrob Agents Chemother. 2015;59(3):1569-1582. doi: 10.1128/AAC.04623-14. PubMed PMID: 25547360; eng.
3. Holmes Edward C, Hurt Aeron C, Dobbie Z, et al. Understanding the Impact of Resistance to Influenza Antivirals. Clinical Microbiology Reviews.34(2):e00224-20. doi: 10.1128/CMR.00224-20.
4. Kiani MA, Ghazanfarpour M, Saeidi M. Influenza: A Unique Disease. International Journal of Pediatrics. 2019;7(4):9349-9354. doi: 10.22038/ijp.2019.37939.3278. en.
5. Gregor J, Radilová K, Brynda J, et al. Structural and Thermodynamic Analysis of the Resistance Development to Pimodivir (VX-787), the Clinical Inhibitor of Cap Binding to PB2 Subunit of Influenza A Polymerase. Molecules. 2021;26(4). doi: 10.3390/molecules26041007.
6. Maheden K, Todd B, Gordon CJ, et al. Inhibition of viral RNA-dependent RNA polymerases with clinically relevant nucleotide analogs. Enzymes. 2021;49:315-354. doi: 10.1016/bs.enz.2021.07.002. PubMed PMID: 34696837; eng.
7. te Velthuis AJW, Fodor E. Influenza virus RNA polymerase: insights into the mechanisms of viral RNA synthesis. Nature Reviews Microbiology. 2016 2016/08/01;14(8):479-493. doi: 10.1038/nrmicro.2016.87.
8. Pflug A, Guilligay D, Reich S, et al. Structure of influenza A polymerase bound to the viral RNA promoter. Nature. 2014 2014/12/01;516(7531):355-360. doi: 10.1038/nature14008.
9. Hayden FG, Shindo N. Influenza virus polymerase inhibitors in clinical development. Current Opinion in Infectious Diseases. 2019;32(2).
10. Reich S, Guilligay D, Pflug A, et al. Structural insight into cap-snatching and RNA synthesis by influenza polymerase. Nature. 2014 2014/12/01;516(7531):361-366. doi: 10.1038/nature14009.
11. Dias A, Bouvier D, Crépin T, et al. The cap-snatching endonuclease of influenza virus polymerase resides in the PA subunit. Nature. 2009 2009/04/01;458(7240):914-918. doi: 10.1038/nature07745.
12. Takashita E. Influenza Polymerase Inhibitors: Mechanisms of Action and Resistance. 2021 May 1, 2021 %J Cold Spring Harbor Perspectives in Medicine;11(5). doi: 10.1101/cshperspect.a038687.
13. Soh YQS, Malone KD, Eguia RT, et al. Comprehensive Profiling of Mutations to Influenza Virus PB2 That Confer Resistance to the Cap-Binding Inhibitor Pimodivir. Viruses. 2021;13(7). doi: 10.3390/v13071196.
14. Finberg RW, Lanno R, Anderson D, et al. Phase 2b Study of Pimodivir (JNJ-63623872) as Monotherapy or in Combination With Oseltamivir for Treatment of Acute Uncomplicated Seasonal Influenza A: TOPAZ Trial. The Journal of Infectious Diseases. 2019;219(7):1026-1034. doi: 10.1093/infdis/jiy547.
15. Patel MC, Chesnokov A, Jones J, et al. Susceptibility of widely diverse influenza a viruses to PB2 polymerase inhibitor pimodivir. Antiviral Research. 2021 2021/04/01/;188:105035. doi: https://doi.org/10.1016/j.antiviral.2021.105035.

16. McGowan DC, Balemans W, Embrechts W, et al. Design, Synthesis, and Biological Evaluation of Novel Indoles Targeting the Influenza PB2 Cap Binding Region. Journal of Medicinal Chemistry. 2019 2019/11/14;62(21):9680-9690. doi: 10.1021/acs.jmedchem.9b01091.
17. Ison MG, Hayden FG, Hay AJ, et al. Influenza polymerase inhibitor resistance: Assessment of the current state of the art - A report of the isirv Antiviral group. Antiviral Research. 2021 2021/10/01/;194:105158. doi: https://doi.org/10.1016/j.antiviral.2021.105158.
18. Trevejo JM, Asmal M, Vingerhoets J, et al. Pimodivir Treatment in Adult Volunteers Experimentally Inoculated with Live Influenza Virus: A Phase IIa, Randomized, Double-Blind, Placebo-Controlled Study. Antiviral Therapy. 2017 2018/05/01;23(4):335-344. doi: 10.3851/IMP3212.
19. Mifsud EJ, Hayden FG, Hurt AC. Antivirals targeting the polymerase complex of influenza viruses. Antiviral Research. 2019 2019/09/01/;169:104545. doi: https://doi.org/10.1016/j.antiviral.2019.104545.
20. Singh R, Bhardwaj VK, Sharma J, et al. Identification of potential plant bioactive as SARS-CoV-2 Spike protein and human ACE2 fusion inhibitors. Computers in Biology and Medicine. 2021 2021/09/01/;136:104631. doi: https://doi.org/10.1016/j.compbiomed.2021.104631.
21. Singh R, Bhardwaj VK, Das P, et al. A computational approach for rational discovery of inhibitors for non-structural protein 1 of SARS-CoV-2. Computers in Biology and Medicine. 2021 2021/08/01/;135:104555. doi: https://doi.org/10.1016/j.compbiomed.2021.104555.
22. Arba M, Wahyudi ST, Brunt DJ, et al. Mechanistic insight on the remdesivir binding to RNA-Dependent RNA polymerase (RdRp) of SARS-cov-2. Computers in Biology and Medicine. 2021 2021/02/01/;129:104156. doi: https://doi.org/10.1016/j.compbiomed.2020.104156.
23. Singh R, Bhardwaj VK, Das P, et al. Benchmarking the ability of novel compounds to inhibit SARS-CoV-2 main protease using steered molecular dynamics simulations. Computers in Biology and Medicine. 2022 2022/07/01/;146:105572. doi: https://doi.org/10.1016/j.compbiomed.2022.105572.
24. Bhardwaj VK, Singh R, Das P, et al. Evaluation of acridinedione analogs as potential SARS-CoV-2 main protease inhibitors and their comparison with repurposed anti-viral drugs. Computers in Biology and Medicine. 2021 2021/01/01/;128:104117. doi: https://doi.org/10.1016/j.compbiomed.2020.104117.
25. Singh R, Bhardwaj VK, Purohit R. Potential of turmeric-derived compounds against RNA-dependent RNA polymerase of SARS-CoV-2: An in-silico approach. Computers in Biology and Medicine. 2021 2021/12/01/;139:104965. doi: https://doi.org/10.1016/j.compbiomed.2021.104965.
26. Sharma J, Kumar Bhardwaj V, Singh R, et al. An in-silico evaluation of different bioactive molecules of tea for their inhibition potency against non structural protein-15 of SARS-CoV-2. Food Chemistry. 2021 2021/06/01/;346:128933. doi: https://doi.org/10.1016/j.foodchem.2020.128933.
27. Thierry E, Guilligay D, Kosinski J, et al. Influenza Polymerase Can Adopt an Alternative Configuration Involving a Radical Repacking of PB2 Domains. Molecular Cell. 2016;61(1):125-137. doi: 10.1016/j.molcel.2015.11.016.
28. Madhavi Sastry G, Adzhigirey M, Day T, et al. Protein and ligand preparation: parameters, protocols, and influence on virtual screening enrichments. Journal of Computer-Aided Molecular Design. 2013 2013/03/01;27(3):221-234. doi: 10.1007/s10822-013-9644-8.
29. Banks JL, Beard HS, Cao Y, et al. Integrated Modeling Program, Applied Chemical Theory (IMPACT) [https://doi.org/10.1002/jcc.20292]. Journal of Computational Chemistry. 2005 2005/12/01;26(16):1752-1780. doi: https://doi.org/10.1002/jcc.20292.
30. Sastry GM, Adzhigirey M, Day T, et al. Protein and ligand preparation: parameters, protocols, and influence on virtual screening enrichments. Journal of Computer-Aided Molecular Design. 2013 Mar;27(3):221-234. doi: 10.1007/s10822-013-9644-8. PubMed PMID: WOS:000318411400002.
31. Liao S, Floyd C, Verratti N, et al. Analysis of vismodegib resistance in D473G and W535L mutants of SMO receptor and design of novel drug derivatives using molecular dynamics simulations. Life Sciences. 2020 2020/03/01/;244:117302. doi: https://doi.org/10.1016/j.lfs.2020.117302.
32. Liao S, Pino MJ, Deleon C, et al. Interaction analyses of hTAAR1 and mTAAR1 with antagonist EPPTB. Life Sciences. 2022 2022/07/01/;300:120553. doi: https://doi.org/10.1016/j.lfs.2022.120553.
33. Friesner RA, Banks JL, Murphy RB, et al. Glide: A new approach for rapid, accurate docking and scoring. 1. Method and assessment of docking accuracy. Journal of Medicinal Chemistry. 2004 Mar;47(7):1739-1749. doi: 10.1021/jm0306430. PubMed PMID: WOS:000220317600019.
34. Friesner RA, Murphy RB, Repasky MP, et al. Extra precision glide: Docking and scoring incorporating a model of hydrophobic enclosure for protein-ligand complexes. Journal of Medicinal Chemistry. 2006 Oct;49(21):6177-6196. doi: 10.1021/jm051256o. PubMed PMID: WOS:000241192400010.

35. Uba AI, Radicella C, Readmond C, et al. Binding of agonist WAY-267,464 and antagonist WAY-methylated to oxytocin receptor probed by all-atom molecular dynamics simulations. Life Sciences. 2020 2020/07/01/;252:117643. doi: https://doi.org/10.1016/j.lfs.2020.117643.
36. Mark P, Nilsson L. Structure and dynamics of the TIP3P, SPC, and SPC/E water models at 298 K. Journal of Physical Chemistry A. 2001 Nov;105(43):9954-9960. doi: 10.1021/jp003020w. PubMed PMID: WOS:000172020100020.
37. Shivakumar D, Williams J, Wu Y, et al. Prediction of Absolute Solvation Free Energies using Molecular Dynamics Free Energy Perturbation and the OPLS Force Field. Journal of Chemical Theory and Computation. 2010 2010/05/11;6(5):1509-1519. doi: 10.1021/ct900587b.
38. Jorgensen WL, Maxwell DS, TiradoRives J. Development and testing of the OPLS all-atom force field on conformational energetics and properties of organic liquids. Journal of the American Chemical Society. 1996 Nov;118(45):11225-11236. doi: 10.1021/ja9621760. PubMed PMID: WOS:A1996VT46600030.
39. Ikeguchi M. Partial rigid-body dynamics in NPT, NPAT and NP gamma T ensembles for proteins and membranes. Journal of Computational Chemistry. 2004 Mar;25(4):529-541. doi: 10.1002/jcc.10402. PubMed PMID: WOS:000189018200006.
40. Bailey AG, Lowe CP. MILCH SHAKE: An Efficient Method for Constraint Dynamics Applied to Alkanes. Journal of Computational Chemistry. 2009 Nov;30(15):2485-2493. doi: 10.1002/jcc.21237. PubMed PMID: WOS:000270869600010.
41. Shan YB, Klepeis JL, Eastwood MP, et al. Gaussian split Ewald: A fast Ewald mesh method for molecular simulation. Journal of Chemical Physics. 2005 Feb;122(5):054101. doi: 10.1063/1.1839571. PubMed PMID: WOS:000226880100002.
42. Stuart SJ, Zhou RH, Berne BJ. Molecular dynamics with multiple time scales: The selection of efficient reference system propagators. Journal of Chemical Physics. 1996 Jul;105(4):1426-1436. doi: 10.1063/1.472005. PubMed PMID: WOS:A1996UY68200014.
43. Kevin J. Bowers EC, Huafeng Xu, Ron O. Dror, Michael P. Eastwood,; Brent A. Gregersen, J. L. K., Istvan Kolossvary, Mark A. Moraes, Federico D. Sacerdoti,; John K. Salmon, Y. S., David E. Shaw. Scalable Algorithms for Molecular Dynamics Simulations on Commodity Clusters. Proceedings of the 2006 ACM/IEEE conference on Supercomputing. 2006:84.
44. Genheden S, Ryde U. The MM/PBSA and MM/GBSA methods to estimate ligand-binding affinities. Expert Opinion on Drug Discovery. 2015 2015/05/04;10(5):449-461. doi: 10.1517/17460441.2015.1032936.
45. Li JN, Abel R, Zhu K, et al. The VSGB 2.0 model: A next generation energy model for high resolution protein structure modeling. Proteins-Structure Function and Bioinformatics. 2011 Oct;79(10):2794-2812. doi: 10.1002/prot.23106. PubMed PMID: WOS:000295428900003.
46. Harder E, Damm W, Maple J, et al. OPLS3: A Force Field Providing Broad Coverage of Drug-like Small Molecules and Proteins. Journal of Chemical Theory and Computation. 2016 2016/01/12;12(1):281-296. doi: 10.1021/acs.jctc.5b00864.
47. Sullivan H-J, Tursi A, Moore K, et al. Binding Interactions of Ergotamine and Dihydroergotamine to 5-Hydroxytryptamine Receptor 1B (5-HT1b) Using Molecular Dynamics Simulations and Dynamic Network Analysis. Journal of Chemical Information and Modeling. 2020 2020/03/23;60(3):1749-1765. doi: 10.1021/acs.jcim.9b01082.
48. Lee C, Yang W, Parr RG. Development of the Colle-Salvetti correlation-energy formula into a functional of the electron density. Physical Review B. 1988 01/15/;37(2):785-789. doi: 10.1103/PhysRevB.37.785.
49. Becke AD. Density-functional thermochemistry. III. The role of exact exchange. The Journal of Chemical Physics. 1993 1993/04/01;98(7):5648-5652. doi: 10.1063/1.464913.
50. Stephens PJ, Devlin FJ, Chabalowski CF, et al. Ab Initio Calculation of Vibrational Absorption and Circular Dichroism Spectra Using Density Functional Force Fields. The Journal of Physical Chemistry. 1994 1994/11/01;98(45):11623-11627. doi: 10.1021/j100096a001.
51. Grimme S, Ehrlich S, Goerigk L. Effect of the damping function in dispersion corrected density functional theory [https://doi.org/10.1002/jcc.21759]. Journal of Computational Chemistry. 2011 2011/05/01;32(7):1456-1465. doi: https://doi.org/10.1002/jcc.21759.
52. Himo F. Quantum chemical modeling of enzyme active sites and reaction mechanisms. Theoretical Chemistry Accounts. 2006 2006/08/01;116(1):232-240. doi: 10.1007/s00214-005-0012-1.
53. Blomberg MRA, Borowski T, Himo F, et al. Quantum Chemical Studies of Mechanisms for Metalloenzymes. Chemical Reviews. 2014 2014/04/09;114(7):3601-3658. doi: 10.1021/cr400388t.

54. Himo F, Siegbahn PEM. Quantum Chemical Studies of Radical-Containing Enzymes. Chemical Reviews. 2003 2003/06/01;103(6):2421-2456. doi: 10.1021/cr020436s.
55. Horn PR, Mao Y, Head-Gordon M. Probing non-covalent interactions with a second generation energy decomposition analysis using absolutely localized molecular orbitals [10.1039/C6CP03784D]. Physical Chemistry Chemical Physics. 2016;18(33):23067-23079. doi: 10.1039/C6CP03784D.
56. Mardirossian N, Head-Gordon M. ωB97M-V: A combinatorially optimized, range-separated hybrid, meta-GGA density functional with VV10 nonlocal correlation. The Journal of Chemical Physics. 2016 2016/06/07;144(21):214110. doi: 10.1063/1.4952647.
57. Weigend F, Ahlrichs R. Balanced basis sets of split valence, triple zeta valence and quadruple zeta valence quality for H to Rn: Design and assessment of accuracy [10.1039/B508541A]. Physical Chemistry Chemical Physics. 2005;7(18):3297-3305. doi: 10.1039/B508541A.
58. Frisch MJ, Trucks GW, Schlegel HB, et al. Gaussian 16 Rev. C.01. Wallingford, CT: 2016.
59. Shao Y, Gan Z, Epifanovsky E, et al. Advances in molecular quantum chemistry contained in the Q-Chem 4 program package. Molecular Physics. 2015 2015/01/17;113(2):184-215. doi: 10.1080/00268976.2014.952696.
60. Glykos NM. Software news and updates carma: A molecular dynamics analysis program [https://doi.org/10.1002/jcc.20482]. Journal of Computational Chemistry. 2006 2006/11/15;27(14):1765-1768. doi: https://doi.org/10.1002/jcc.20482.